

## Effective removal of Pb<sup>2+</sup> and Cd<sup>2+</sup> from wastewater by mesoporous tobermorite synthesized from alumina-extracted fly ash

Zehua Wang<sup>a</sup>, Zhongliang Huang<sup>a</sup>, Shili Zheng<sup>b</sup>, Daishe Wu<sup>a,\*</sup>, Weiquan Cai<sup>c,d,\*</sup>

<sup>a</sup>School of Resources Environmental & Chemical Engineering, Key Laboratory of Poyang Lake Environmental and Resource Utilization, Ministry of Education, Nanchang University, Nanchang 330031, China, Tel. +86 79183968330; Fax: +86 79183968330; email: dswu@ncu.edu.cn

<sup>b</sup>National Engineering Laboratory for Hydrometallurgy Cleaner Production Technology, Key Laboratory of Green Process and Engineering, Institute of Process Engineering, Chinese Academy of Sciences, Beijing 100190, China

<sup>c</sup>School of Chemistry and Chemical Engineering, Guangzhou University, Guangzhou 510006, China, Tel. +86 2039366902; Fax: +86 2039366902; email: cccaiwq@gzhu.edu.cn

<sup>d</sup>School of Materials Science and Engineering, Zhengzhou University, Zhengzhou, 450002, China

Received 10 May 2021; Accepted 23 July 2021

### ABSTRACT

In this study, for the first time, the effective removal of Pb<sup>2+</sup> and Cd<sup>2+</sup> from wastewater by mesoporous tobermorite synthesized from alumina-extracted fly ash (AEFA) was reported. The results of characterization of the synthesized tobermorite indicated that it showed mesoporous structure, with a high specific surface area of 68.4 m<sup>2</sup> g<sup>-1</sup>. The tobermorite particles were aggregates of plate-like particles resulting in slit-shaped pores. The mesoporous tobermorite showed high removal efficiency for Pb<sup>2+</sup> and Cd<sup>2+</sup> of 99.97% and 78.64%, respectively, and the adsorption kinetic data for Pb<sup>2+</sup> and Cd<sup>2+</sup> on tobermorite were better fitted to the pseudo-second-order kinetic model. The Pb<sup>2+</sup> and Cd<sup>2+</sup> adsorption isotherms were better described by the Langmuir isotherm model, and the maximum adsorption capacities of the tobermorite towards Pb<sup>2+</sup> and Cd<sup>2+</sup> were 338.98 and 105.37 mg g<sup>-1</sup>, respectively. The high adsorption capacities of the tobermorite towards Pb<sup>2+</sup> and Cd<sup>2+</sup> were due to its high specific surface area, the ion exchange of Ca<sup>2+</sup> with Pb<sup>2+</sup> and Cd<sup>2+</sup>, and the precipitation. This study shows the mesoporous tobermorite synthesized from AEFA as a low-cost and effective adsorbent for Pb<sup>2+</sup> and Cd<sup>2+</sup> and broadens the potential application of AEFA in wastewater treatment.

*Keywords:* Fly ash; Tobermorite; Adsorption; Heavy metal; Pb<sup>2+</sup>; Cd<sup>2+</sup>

### 1. Introduction

Water pollution has become a serious environmental problem along with the development of the industry. Heavy metal pollution is one of the most urgent issues, because heavy metals in aqueous solutions are very toxic and non-biodegradable, accumulating through the food chain and affecting human health [1–3]. Lead is widely used in industrial processes such as lead-acid batteries, printing, painting, metal products and other industries, and it

can cause kidney disease, mental retardation, and nervous system damage [2–4]. Cadmium is used as stabilizers in nickel-cadmium batteries, alloys, color pigment, PVC products, and phosphate fertilizers, and it can cause kidney damage, skeletal damage, and cancer [2–4]. Many methods have been used to remove Pb<sup>2+</sup> and Cd<sup>2+</sup> from wastewater, such as chemical precipitation, coagulation, adsorption, ion exchange, membrane filtration, electrolysis, phytoremediation, etc. [5–8]. Among them, adsorption has many advantages, such as simplicity of operation and high efficiency [9].

\* Corresponding author.

Various adsorbents have been developed to remove  $\text{Pb}^{2+}$  and  $\text{Cd}^{2+}$  from aqueous solution efficiently, including alumina [10,11], carbon nanotube [12,13], graphene [14,15], activated carbon [16,17], zeolite [18,19], etc. Although these adsorbents show good adsorption capacities, their high costs of preparation limit their application. In recent years, a number of researchers have investigated solid wastes for adsorbing  $\text{Pb}^{2+}$  and  $\text{Cd}^{2+}$  from wastewater, due to their low cost [20,21].

Fly ash is an industrial solid waste generated by the combustion of coal in coal-fired power plants, with an enormous annual output of approximately 580, 160, and 130 million tons in China, India, and the US in 2015, respectively [22]. High-alumina fly ash is a type of fly ash with an alumina content of higher than 35 wt.% [23–25], which can be used to produce alumina by a mild hydro-chemical process, generating  $\text{NaAlO}_2$  solution and the alumina-extracted fly ash (AEFA) [26,27]. Our previous works have successfully used the AEFA to synthesize tobermorite in alkaline solution [28,29]. Tobermorite is a type of crystalline calcium silicate hydrate and it has good adsorption performance for heavy metal ions [30–33]. It is reasonable to speculate that the tobermorite synthesized from AEFA has potential application in the removal of  $\text{Pb}^{2+}$  and  $\text{Cd}^{2+}$  from wastewater. However, there are few studies about the adsorption abilities and adsorption mechanisms of  $\text{Pb}^{2+}$  and  $\text{Cd}^{2+}$  by the tobermorite synthesized from AEFA.

In this study, the mineralogical, chemical, structural, and morphological properties of the tobermorite synthesized from AEFA were characterized by X-ray diffraction (XRD), inductively coupled plasma-optical emission spectrometry (ICP-OES), nuclear magnetic resonance (NMR), Brunauer–Emmett–Teller (BET) specific surface area analyzer, scanning electron microscopy (SEM), and transmission electron microscopy-energy-dispersive X-ray spectroscopy (TEM-EDS). For the first time, the adsorption performance of the tobermorite synthesized from AEFA towards  $\text{Pb}^{2+}$  and  $\text{Cd}^{2+}$  was investigated by kinetic and isotherm studies. The tobermorite synthesized from AEFA showed high adsorption capacities of  $\text{Pb}^{2+}$  and  $\text{Cd}^{2+}$ , which were 338.98 and 105.37  $\text{mg g}^{-1}$ , respectively. The tobermorite after adsorption of  $\text{Pb}^{2+}$  and  $\text{Cd}^{2+}$  were analyzed by XRD, SEM-EDS and X-ray photoelectron spectroscopy (XPS), to reveal the adsorption mechanisms. The aim of this study was to realize the resource utilization of tobermorite synthesized from AEFA as an effective and low-cost adsorbent towards  $\text{Pb}^{2+}$  and  $\text{Cd}^{2+}$  in wastewater.

## 2. Experimental section

### 2.1. Materials

The AEFA, whose main crystalline phase was  $\text{NaCaHSiO}_4$ , obtained by extracting alumina from the high-alumina fly ash using a hydro-chemical process [26,27]. This process was conducted at 260°C to leach alumina from high-alumina fly ash using concentrated NaOH solution and CaO with C/S (mass ratio of CaO to  $\text{SiO}_2$ ) of 1.0. The main components of the AEFA used in this study were  $\text{Na}_2\text{O}$  (16.15 wt.%), CaO (32.43 wt.%), and  $\text{SiO}_2$  (32.96 wt.%). The sodium hydroxide, lead nitrate, cadmium chloride, and hydrochloric acid were of analytical grade, purchased from China Xilong Chemical Co., Ltd. The high-purity Milli-Q water was used for all experiments.

### 2.2. Preparation of tobermorite

The preparation of tobermorite from AEFA was using a hydrothermal method according to our previous study [28]. In detail, the mixture of AEFA and NaOH solution (20  $\text{g L}^{-1}$   $\text{Na}_2\text{O}$ ), whose liquid to solid ratio was 20  $\text{mL g}^{-1}$ , were added into a 1 L autoclave. Then, they were digested at 170°C for 4 h under stirring. After the reaction, the slurry was filtered and washed with heated deionized water 3 times to reduce the adsorption of sodium ions on the structure of the product. Eventually, the synthesized product was dried in an oven at 80°C for 12 h.

### 2.3. $\text{Pb}^{2+}$ and $\text{Cd}^{2+}$ adsorption

Batch adsorption experiments of  $\text{Pb}^{2+}$  and  $\text{Cd}^{2+}$  were performed in 50 mL centrifuge tubes.  $\text{Pb}(\text{NO}_3)_2$  and  $\text{CdCl}_2$  were dissolved in deionized water to prepare  $\text{Pb}^{2+}$  and  $\text{Cd}^{2+}$  solutions, respectively. The pH of the  $\text{Pb}^{2+}$  and  $\text{Cd}^{2+}$  solutions with the concentration of 100  $\text{mg L}^{-1}$  were adjusted to 2–7 using 0.1 M HCl or NaOH solutions, respectively. The higher pH values of the solutions were not used to avoid precipitation. In a typical experiment, 0.02 g synthesized products were added into 20 mL  $\text{Pb}^{2+}$  or  $\text{Cd}^{2+}$  solutions with the concentration of 100  $\text{mg L}^{-1}$  and different pH values, shaken at room temperature for 1 h. Then, the  $\text{Pb}^{2+}$  or  $\text{Cd}^{2+}$  solutions were filtered through a syringe filter (0.45  $\mu\text{m}$ ) and the residual concentration of  $\text{Pb}^{2+}$  or  $\text{Cd}^{2+}$  in the solutions was measured by the ICP-OES.

In order to investigate the adsorption kinetics, 0.02 g synthesized product was added into 20 mL  $\text{Pb}^{2+}$  or  $\text{Cd}^{2+}$  solution with a pH of 4 or 5 and the concentration of 100  $\text{mg L}^{-1}$ , shaken at room temperature for different time intervals. Then, the  $\text{Pb}^{2+}$  or  $\text{Cd}^{2+}$  concentrations in the solutions with different adsorption time were measured.

To study adsorption isotherm, 0.02 g synthesized products and 20 mL  $\text{Pb}^{2+}$  or  $\text{Cd}^{2+}$  solutions with the pH of 4 or 5 and different concentrations (100, 200, 300, 400, 500, 600, and 1,000  $\text{mg L}^{-1}$ ) were shaken for 1 h at room temperature. Then, the  $\text{Pb}^{2+}$  or  $\text{Cd}^{2+}$  concentration in the solutions after adsorption were analyzed.

To investigate the adsorption abilities of the synthesized product towards the mixture of metal ions, 0.1 g synthesized products and 100 mL solution of a mixture of metal ions, including  $\text{Pb}^{2+}$ ,  $\text{Cd}^{2+}$ ,  $\text{Mg}^{2+}$ ,  $\text{Zn}^{2+}$ , and  $\text{Mn}^{2+}$ , were shaken at room temperature for different time intervals. The concentration of each metal ion in the solution was 50  $\text{mg L}^{-1}$ . Then, the concentration of  $\text{Pb}^{2+}$ ,  $\text{Cd}^{2+}$ ,  $\text{Mg}^{2+}$ ,  $\text{Zn}^{2+}$ , and  $\text{Mn}^{2+}$  in the solutions with different adsorption time were measured by ICP-OES.

The products after adsorption of  $\text{Pb}^{2+}$  or  $\text{Cd}^{2+}$  were washed with deionized water three times and dried at 80°C for further characterization.

### 2.4. Characterization

The synthesized product and the products after adsorption were characterized by X-ray diffraction (XRD, X'Pert Pro MPD, PANalytical) for identifying the mineral phases. The chemical composition of the product and the concentration of  $\text{Pb}^{2+}$  or  $\text{Cd}^{2+}$  in aqueous solution were analyzed using inductively coupled plasma-optical emission spectrometry

(ICP-OES; Optimal 7300 V, PerkinElmer Instruments, USA). The silicate structure of the product was analyzed by  $^{29}\text{Si}$  magic-angle spinning nuclear magnetic resonance (MAS NMR, Bruker AVANCE III 400 MHz, Switzerland). The  $\text{N}_2$  adsorption–desorption isotherm of the product was measured by a specific surface area analyzer (ASAP 2020 HD88), the pore size distribution was determined by the Barrett–Joyner–Halenda method and the specific surface area was calculated from BET equations. The morphology and microstructure of the product were observed by scanning electron microscopy (SEM, JSM-7100F). Transmission electron microscopy (TEM) images, high angle annular dark-field scanning transmission electron microscopy (HAADF-STEM) images, and energy-dispersive X-ray spectrometer (EDS) elemental mapping were recorded by the high-resolution transmission electron microscopy (HRTEM, JEM-2100F). The morphology and the elemental analysis of the products after adsorption of  $\text{Pb}^{2+}$  or  $\text{Cd}^{2+}$  were conducted by SEM-EDS (JSM-6701F). The elements of the products after adsorption of  $\text{Pb}^{2+}$  or  $\text{Cd}^{2+}$  were analyzed by X-ray photoelectron spectroscopy (XPS, ESCALAB250Xi, Thermo Fisher Scientific).

### 3. Results and discussion

#### 3.1. Characterization of the synthesized product

The XRD pattern of the synthesized product is shown in Fig. 1. The main diffraction peaks at about  $7.7^\circ$ ,  $16.3^\circ$ ,  $29.0^\circ$ ,  $31.8^\circ$ ,  $49.4^\circ$  were indexed to tobermorite ( $\text{Ca}_5(\text{OH})_2\text{Si}_6\text{O}_{16}\cdot 4\text{H}_2\text{O}$ , ICDD card no. 00-019-1364), suggesting the main mineral phase of the synthesized product was tobermorite. The main chemical compositions of the synthesized product were  $\text{SiO}_2$  and  $\text{CaO}$ , as shown in Table 1. The C/S (the mass ratio of  $\text{CaO}$  to  $\text{SiO}_2$ ) of the product was 0.91, which was only a little bit higher than that of tobermorite. This reveals that the product was mainly composed of tobermorite.

To investigate the structure of the synthesized product, the  $^{29}\text{Si}$  MAS NMR spectrum of the tobermorite was studied, which is shown in Fig. 2. According to the literature, the tobermorite has a sandwich-like structure that consists of a central layer of  $\text{CaO}$  octahedra with individual silicate “dreierketten” chains on each side [34]. In this study, there

were four peaks for the end of the silicate “dreierketten” chain ( $\text{Q}^1$ ), the bridging site ( $\text{Q}_\text{B}^2$ ), the pairing site ( $\text{Q}_\text{P}^2$ ), and the branching site ( $\text{Q}^3$ ) at about  $-79$ , about  $-82$ , about  $-85$ , and about  $-95$  ppm, respectively. These values were similar to our previous  $^{29}\text{Si}$  MAS NMR studies of the hydrothermally synthesized tobermorite samples [34]. The appearance of the characteristic peak of the branching site  $\text{Q}^3$  confirmed the formation of the cross-linked structure of tobermorite.

The textural properties of the tobermorite were measured by  $\text{N}_2$  adsorption–desorption. Fig. 3a shows that the  $\text{N}_2$  adsorption–desorption isotherm of the tobermorite was of type IV with H3 hysteresis loop, indicating that it was mesoporous material and the pore structure was slit-shaped pores resulting from the aggregates of plate-like particles [31]. Fig. 3b presents the pore size distribution curve of the tobermorite, which centered at about 5 nm, also confirming that the tobermorite was mesoporous material. The calculated BET specific surface area of the tobermorite synthesized from AEFA in this study was  $68.4 \text{ m}^2 \text{ g}^{-1}$ , which was higher than that of the previously reported tobermorite synthesized from municipal solid waste incineration bottom ash ( $26.9 \text{ m}^2 \text{ g}^{-1}$ ) [31], the tobermorite synthesized from quartz ( $67.04 \text{ m}^2 \text{ g}^{-1}$ ) [32], and the tobermorite synthesized from blast furnace slag at  $180^\circ\text{C}$  for 48 h ( $51 \text{ m}^2 \text{ g}^{-1}$ ) [33], but it was lower than those of the tobermorite synthesized from blast furnace slag at  $180^\circ\text{C}$  for 2 h ( $72 \text{ m}^2 \text{ g}^{-1}$ ) and 3 h ( $92 \text{ m}^2 \text{ g}^{-1}$ ) [33]. In addition, the pore volume of the tobermorite in this study was  $0.19 \text{ cm}^3 \text{ g}^{-1}$ . The high specific

Table 1  
Chemical composition of the synthesized product

Composition	Content (wt.%)
$\text{Al}_2\text{O}_3$	2.07
$\text{SiO}_2$	36.64
$\text{CaO}$	33.43
$\text{Na}_2\text{O}$	2.56
A/S	0.06
C/S	0.91

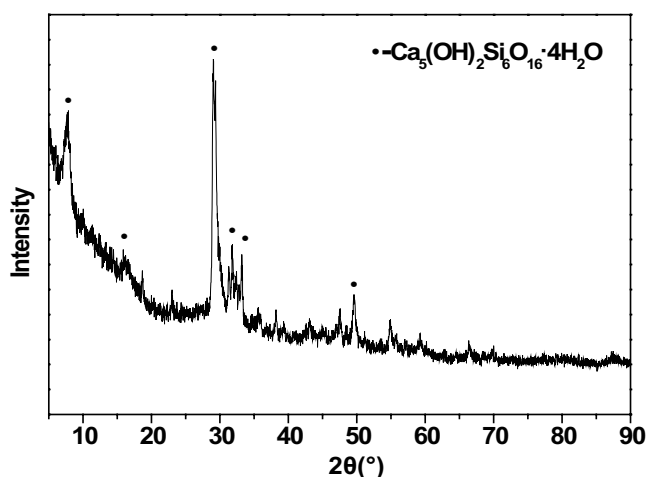


Fig. 1. XRD pattern of the synthesized product.

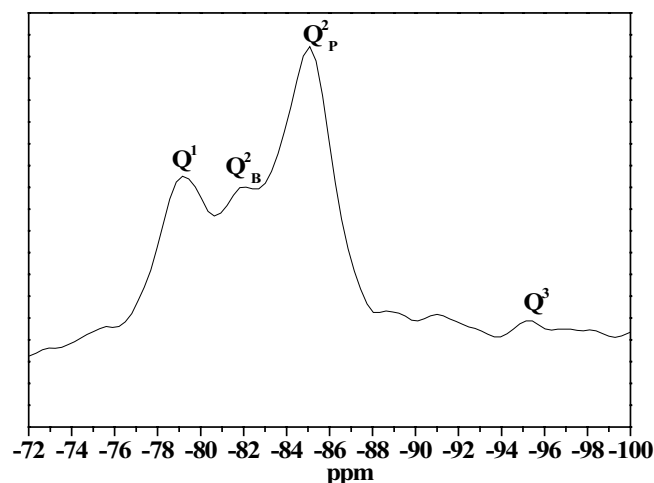


Fig. 2.  $^{29}\text{Si}$  MAS NMR spectrum of the product.

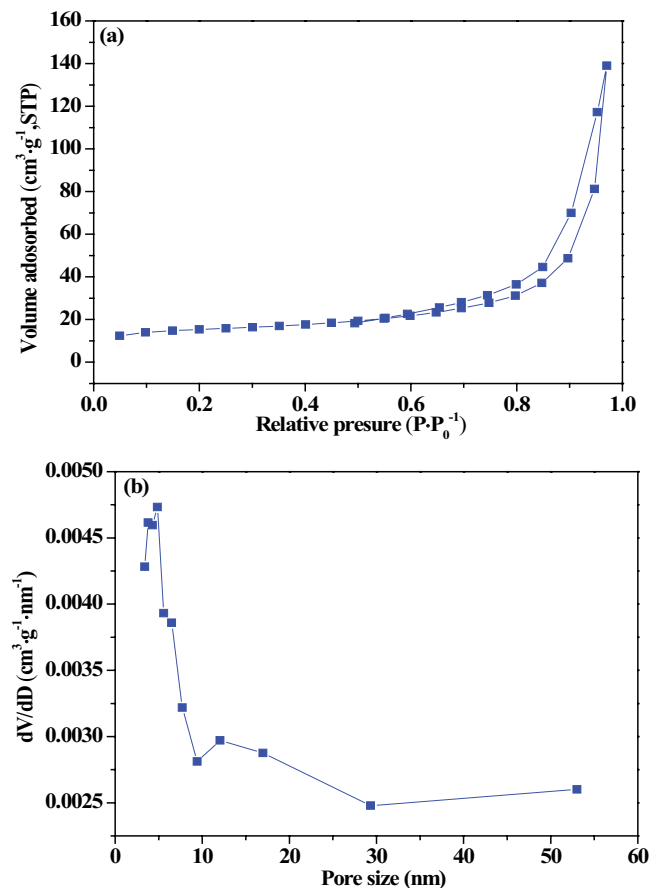


Fig. 3.  $N_2$  adsorption–desorption isotherm (a) and pore size distribution curve (b) of the tobermorite.

surface area of the tobermorite synthesized from AEFA in this study might result in the high adsorption capacity of heavy metals.

The morphology of the tobermorite was characterized by SEM. Fig. 4a and b show SEM images of the tobermorite particles, indicating that the tobermorite particles were in the size of dozens of micrometers and they were aggregates of plate-like particles forming slit-shaped pores, which was consistent with the result of  $N_2$  adsorption-desorption isotherm. Fig. 4c–f presents the HAADF-STEM image and EDS elemental mapping of the tobermorite, revealing that the primary morphology of the tobermorite was nanosheet, mainly consisted of O, Si, and Ca. During the reaction, the nanosheets aggregated together to form mesoporous micrometer particles under stirring, due to the cross-linking of silicate chains. Above all, the porous morphology of the tobermorite might result in a good adsorption ability of heavy metals.

### 3.2. Adsorption

#### 3.2.1. Effect of pH

The pH of the solution is of great importance to the adsorption of heavy metals from an aqueous solution, because the pH affects both the heavy metal ionic state and the properties of the adsorbent. The effects of pH on

the removal efficiency of  $Pb^{2+}$  and  $Cd^{2+}$  on tobermorite are shown in Fig. 5. The removal efficiencies of  $Pb^{2+}$  and  $Cd^{2+}$  increased from 61.12% and 36.69% to 99.94% and 69.00%, respectively when pH increased from 2 to 3, and then the adsorption was almost saturated. When the pH was lower than 3, a large amount of  $H^+$  was released and the cation exchange of  $H^+$  with  $Pb^{2+}$  and  $Cd^{2+}$  occurred, which inhibited the adsorption of  $Pb^{2+}$  and  $Cd^{2+}$  on tobermorite. The maximum removal efficiencies of  $Pb^{2+}$  and  $Cd^{2+}$  on tobermorite were 99.97% at pH 4 and 78.64% at pH 5, respectively. Therefore, pH 4 and pH 5 were chosen for the following adsorption experiments of  $Pb^{2+}$  and  $Cd^{2+}$ , respectively.

#### 3.2.2. Adsorption kinetics

The removal efficiency vs. time for  $Pb^{2+}$  and  $Cd^{2+}$  adsorption on tobermorite is shown in Fig. 6a. Obviously, the adsorption rate for  $Pb^{2+}$  on tobermorite was faster than that for  $Cd^{2+}$ . The removal efficiencies for  $Pb^{2+}$  and  $Cd^{2+}$  on tobermorite at 2 min were 99.6% and 37.8%, respectively. Then,  $Pb^{2+}$  and  $Cd^{2+}$  were adsorbed slowly to reach equilibrium with the removal efficiencies of 99.97% (adsorption capacity of 99.97  $mg\ g^{-1}$ ) and 78.64% (adsorption capacity of 78.64  $mg\ g^{-1}$ ), respectively.

The kinetic data for  $Pb^{2+}$  and  $Cd^{2+}$  adsorption on tobermorite were fitted by the pseudo-first-order and pseudo-second-order models. The equations were as follows [35,36]:

The pseudo-first-order model:

$$\ln(q_e - q_t) = \ln q_e - k_1 t \quad (1)$$

The pseudo-second-order model:

$$\frac{t}{q_t} = \frac{1}{k_2 q_e^2} + \frac{t}{q_e} \quad (2)$$

where  $t$  is time,  $q_e$  and  $q_t$  are the adsorption capacity at equilibrium and at time  $t$ , respectively, and  $k_1$  is the rate constant of the pseudo-first-order model,  $k_2$  is the rate constant of the pseudo-second-order model.

The fitting parameters of the two kinetic models for  $Pb^{2+}$  and  $Cd^{2+}$  adsorption on tobermorite are given in Table 2. The results suggest that the adsorption kinetic data for  $Pb^{2+}$  and  $Cd^{2+}$  on tobermorite were better fitted to the pseudo-second-order kinetic model, with a correlation coefficient of 1.000 and 0.998, respectively, which reveals that this adsorption process was governed by chemisorption involving valence forces through the sharing or exchange of electrons between the tobermorite and  $Pb^{2+}/Cd^{2+}$  as covalent forces [35,36].

#### 3.2.3. Adsorption isotherms

The adsorption isotherms for  $Pb^{2+}$  and  $Cd^{2+}$  on tobermorite are shown in Fig. 7. The equilibrium adsorption capacities of tobermorite towards  $Pb^{2+}$  and  $Cd^{2+}$  gradually increased with the initial concentration of  $Pb^{2+}$  and  $Cd^{2+}$  and then reached a saturation value. Both the Langmuir isotherm model and Freundlich isotherm model were used to analyze the adsorption data. The equations were as follows.

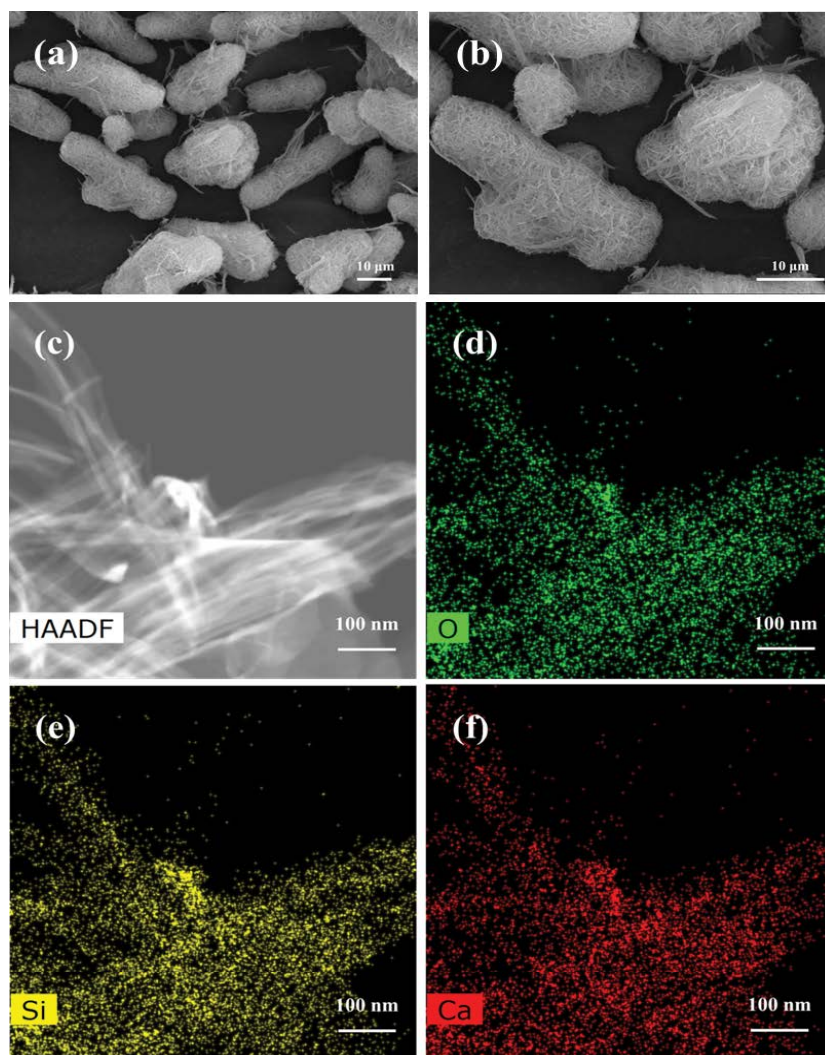


Fig. 4. SEM images (a,b), HAADF-STEM image (c) and EDS elemental mapping (d–f) of the tobermorite.

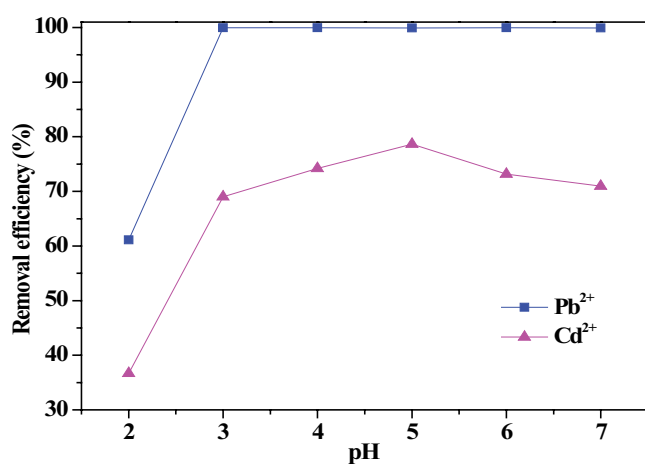


Fig. 5. Effects of pH on the removal efficiencies of Pb<sup>2+</sup> and Cd<sup>2+</sup> on tobermorite.

The Langmuir isotherm model:

$$\frac{C_e}{q_e} = \frac{1}{k_L q_m} + \frac{C_e}{q_m} \quad (3)$$

The Freundlich isotherm model:

$$\ln q_e = \frac{1}{n} \ln C_e + \ln k_f \quad (4)$$

where  $C_e$  is the equilibrium concentration of Pb<sup>2+</sup> and Cd<sup>2+</sup> in solution,  $q_e$  is the equilibrium adsorption capacity,  $q_m$  is the maximum adsorption capacity,  $k_L$  is the Langmuir adsorption constant,  $k_f$  and  $n$  are the Freundlich adsorption constants related to adsorption capacity and adsorption intensity.

As shown in Fig. 7 and Table 3, the Pb<sup>2+</sup> and Cd<sup>2+</sup> adsorption data were better described by the Langmuir isotherm model, with the higher correlation coefficients of 0.999 and 0.998, respectively, suggesting monolayer adsorption of Pb<sup>2+</sup> and Cd<sup>2+</sup> on tobermorite, and this was consistent

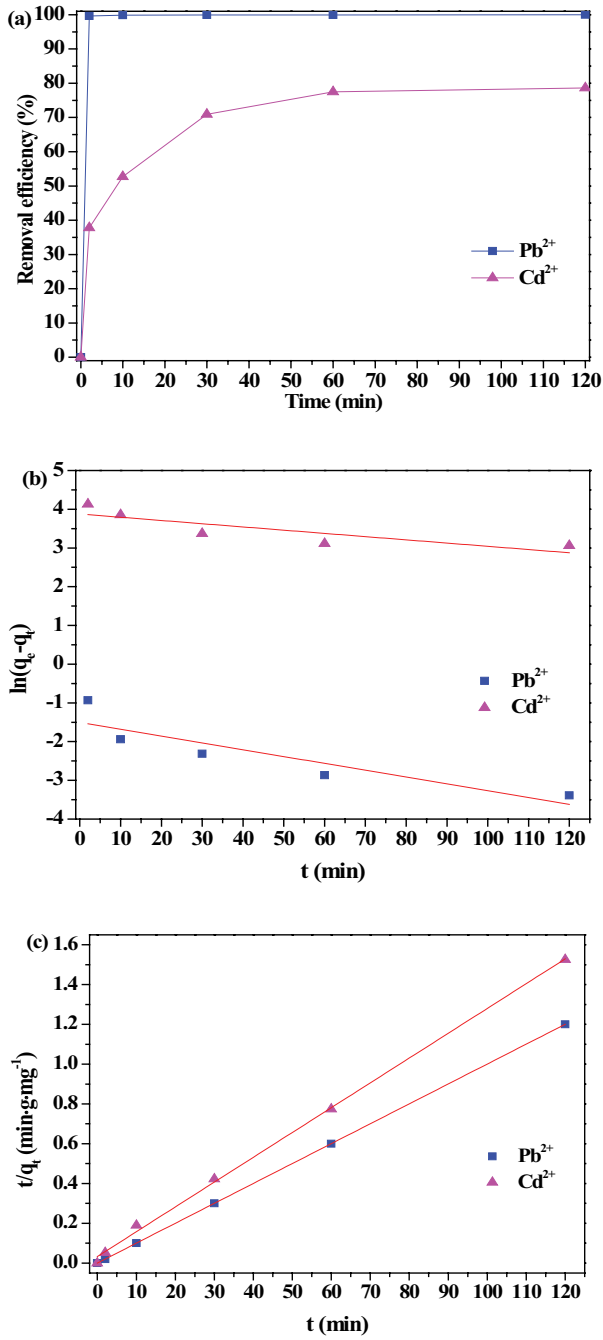


Fig. 6. Removal efficiency vs. time (a), pseudo-first-order kinetic model (b), and pseudo-second-order kinetic model (c) for Pb<sup>2+</sup> and Cd<sup>2+</sup> adsorption on tobermorite.

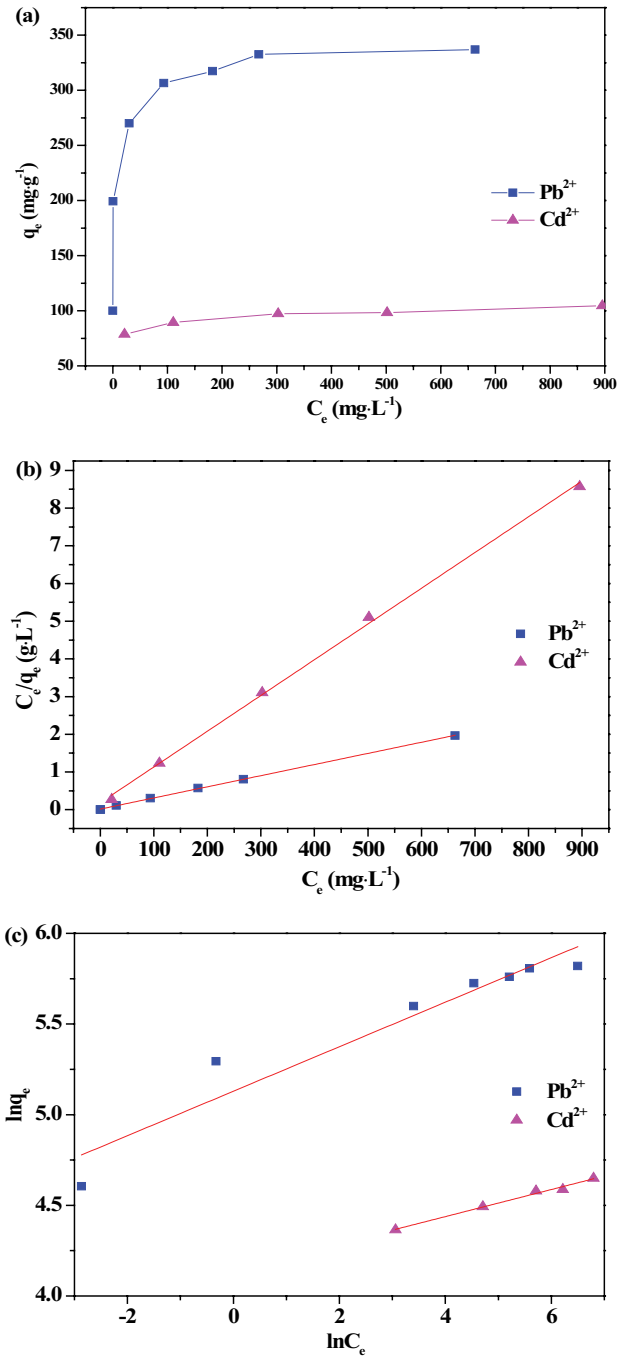


Fig. 7. Adsorption isotherms (a), Langmuir model (b), and Freundlich model (c) for Pb<sup>2+</sup> and Cd<sup>2+</sup> on tobermorite.

Table 2  
Parameters for Pb<sup>2+</sup> and Cd<sup>2+</sup> adsorption kinetics on tobermorite

Metal ion	Q <sub>e,exp</sub> (mg g <sup>-1</sup> )	Pseudo-first-order model			Pseudo-second-order model		
		Q <sub>e,cal</sub> (mg g <sup>-1</sup> )	k <sub>1</sub> (min <sup>-1</sup> )	R <sup>2</sup>	Q <sub>e,cal</sub> (mg g <sup>-1</sup> )	k <sub>2</sub> (g mg <sup>-1</sup> min <sup>-1</sup> )	R <sup>2</sup>
Pb <sup>2+</sup>	99.97	0.23	0.0351	0.950	100.00	1.0117	1.000
Cd <sup>2+</sup>	78.64	73.75	0.0835	0.975	80.19	0.0047	0.998

with the previous reports for the adsorption of  $\text{Cd}^{2+}$  and  $\text{Cr(VI)}$  on tobermorite [30,32]. The fitting results also indicate that the maximum adsorption capacities ( $q_m$ ) for  $\text{Pb}^{2+}$  and  $\text{Cd}^{2+}$  on tobermorite synthesized from AEFA were 338.98 and 105.37  $\text{mg g}^{-1}$ , respectively. The  $q_m$  for  $\text{Pb}^{2+}$  on tobermorite synthesized from AEFA was much higher than that for  $\text{Cd}^{2+}$ , which might be due to the smaller hydrated ionic radius of  $\text{Pb}^{2+}$  than that of  $\text{Cd}^{2+}$  [37–40]. Compared with  $\text{Cd}^{2+}$ ,  $\text{Pb}^{2+}$  was easier to diffuse into the pores of the synthesized mesoporous tobermorite, resulting in a higher  $q_m$  of  $\text{Pb}^{2+}$  than that of  $\text{Cd}^{2+}$ . The comparisons of adsorption capacity for  $\text{Pb}^{2+}$  and  $\text{Cd}^{2+}$  on various adsorbents are shown in Tables 4 and 5, respectively. As shown in Table 4, the  $q_m$  for  $\text{Pb}^{2+}$  on tobermorite synthesized from AEFA in this study was higher than those for  $\text{Pb}^{2+}$  on alumina [10,11], carbon nanotube [12,13], graphene [14,15], activated carbon [16,17], zeolite [18,19], ligand-based composite [41], Ti(IV) iodovanadate cation exchanger [42], fly ash [43,44], zeolite from fly ash [45,46], and Al-substituted tobermorite from newsprint recycling residue [47], all of which are without functionalization. As shown in Table 5, the  $q_m$  for

$\text{Cd}^{2+}$  on tobermorite synthesized from AEFA in this study was higher than those for  $\text{Cd}^{2+}$  on alumina [10], activated carbon [48], fly ash [49], modified fly ash [50], zeolite [51], zeolite from fly ash [45,46], and Al-substituted tobermorite from newsprint recycling residue [47], but it was lower than those for  $\text{Cd}^{2+}$  on activated carbon/ZrO<sub>2</sub> composite [52] and tobermorite from newsprint recycling residue [30]. The high adsorption capacity of the synthesized tobermorite might be due to the mesoporous structure, high specific surface area, and the natural properties of the tobermorite. The  $\text{Ca}^{2+}$  from the interlayer and the structure of tobermorite could exchange with the  $\text{Pb}^{2+}$  and  $\text{Cd}^{2+}$  ions which diffused into the structure of the mesoporous tobermorite, leading to the high adsorption capacity of  $\text{Pb}^{2+}$  and  $\text{Cd}^{2+}$  [32]. The high adsorption capacities for  $\text{Pb}^{2+}$  and  $\text{Cd}^{2+}$  on the tobermorite indicate that the tobermorite synthesized from alumina-extracted fly ash has a good application prospect as a low-cost and efficient adsorbent for  $\text{Pb}^{2+}$  and  $\text{Cd}^{2+}$  in wastewater.

A variety of heavy metal ions might coexist in real wastewater and compete for active sites. Therefore, the adsorption abilities of the tobermorite synthesized from AEFA in this study towards a mixture of metal ions, including  $\text{Pb}^{2+}$ ,  $\text{Cd}^{2+}$ ,  $\text{Mg}^{2+}$ ,  $\text{Zn}^{2+}$ , and  $\text{Mn}^{2+}$ , were investigated. The results are shown in Fig. 8, the removal efficiencies of  $\text{Pb}^{2+}$  and  $\text{Cd}^{2+}$  on the tobermorite were higher than those of  $\text{Mg}^{2+}$ ,  $\text{Zn}^{2+}$ , and  $\text{Mn}^{2+}$ . What is noteworthy is that the adsorption rate and adsorption capacity of  $\text{Pb}^{2+}$  on the tobermorite were fastest and highest, respectively, among the mixture of metal ions, which might be due to the small hydrated ionic radius and low hydration energy of  $\text{Pb}^{2+}$  [37–40].

Table 3  
Parameters for  $\text{Pb}^{2+}$  and  $\text{Cd}^{2+}$  adsorption isotherms on tobermorite

Metal ion	Langmuir			Freundlich		
	$q_m$ ( $\text{mg g}^{-1}$ )	$k_L$ ( $\text{L mg}^{-1}$ )	$R^2$	$n$	$k_f$	$R^2$
$\text{Pb}^{2+}$	338.98	0.183	0.999	8.149	168.9	0.909
$\text{Cd}^{2+}$	105.37	0.0519	0.998	13.40	62.76	0.988

Table 4  
Comparison of adsorption capacities of  $\text{Pb}^{2+}$  on various adsorbents

Adsorbent	$q_m$ ( $\text{mg g}^{-1}$ )	Reference
Alumina	83.33	[10]
Alumina	125.00	[11]
Carbon nanotube	49.95	[12]
Carbon nanotube	117.65	[13]
Graphene	35.46	[14]
Graphene	80.00	[15]
Activated carbon	29.44	[16]
Activated carbon	27.53	[17]
Zeolite	68.00	[18]
Zeolite	20.10	[19]
Ligand based composite	214.15	[41]
Ti(IV) iodovanadate cation exchanger	18.80	[42]
Fly ash	22.00	[43]
Fly ash	18.00	[44]
Zeolite from fly ash	98.04	[45]
Zeolite from fly ash	65.75	[46]
Al-substituted tobermorite from newsprint recycling residue	1.99	[47]
Tobermorite from AEFA	338.98	This study

### 3.2.4. Adsorption mechanisms

To better understand the adsorption mechanisms, the concentrations of  $\text{Pb}^{2+}$  and  $\text{Ca}^{2+}$ ,  $\text{Cd}^{2+}$  and  $\text{Ca}^{2+}$  in the solution vs. time were analyzed, respectively. Fig. 9 shows a nearly equal molar amount of the adsorbed  $\text{Pb}^{2+}$  and  $\text{Cd}^{2+}$  with the molar amount of  $\text{Ca}^{2+}$  released in the solution. This reveals that  $\text{Pb}^{2+}$  and  $\text{Cd}^{2+}$  were adsorbed by ion exchange with  $\text{Ca}^{2+}$

Table 5  
Comparison of adsorption capacities of  $\text{Cd}^{2+}$  on various adsorbents

Adsorbent	$q_m$ ( $\text{mg g}^{-1}$ )	Reference
Alumina	25.06	[10]
Activated carbon	1.85	[48]
Fly ash	18.98	[49]
Modified fly ash	56.31	[50]
Zeolite	1.89	[51]
Zeolite from fly ash	26.88	[45]
Zeolite from fly ash	52.12	[46]
Al-substituted tobermorite from newsprint recycling residue	2.00	[47]
Activated carbon/ZrO <sub>2</sub> composite	166.70	[52]
Tobermorite from newsprint recycling residue	179.00	[30]
Tobermorite from AEFA	105.37	This study

in the structure of tobermorite [32]. However, the molar amount of  $\text{Ca}^{2+}$  released in the solution was a little bit higher than that of  $\text{Pb}^{2+}$  adsorbed on tobermorite, indicating that the  $\text{Ca}^{2+}$  released in the solution might be attributed to both

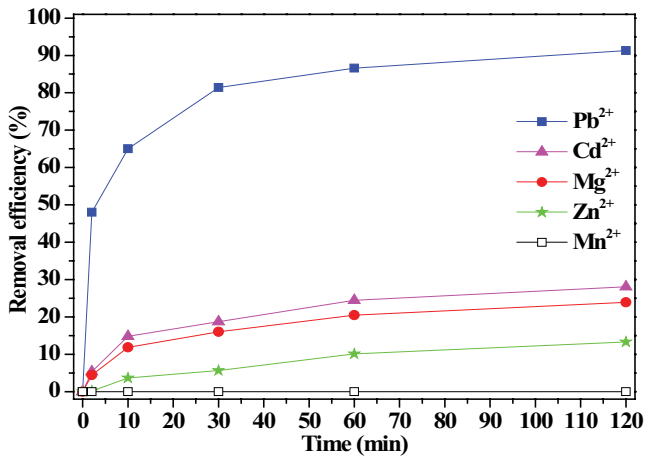


Fig. 8. Removal efficiency vs. time of mixture of metal ions on tobermorite.

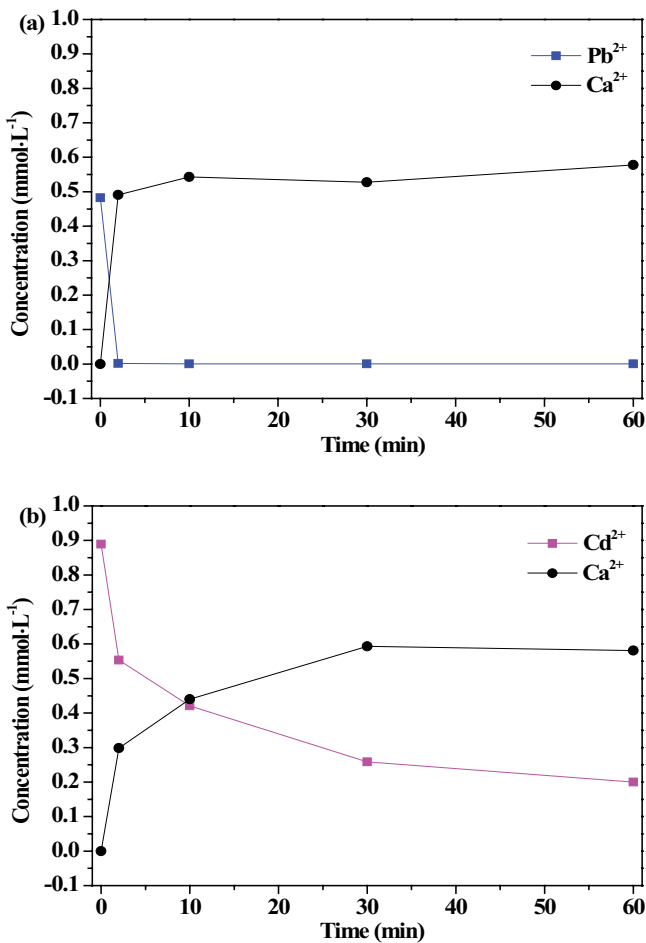


Fig. 9. The concentrations of  $\text{Pb}^{2+}$  and  $\text{Ca}^{2+}$  (a),  $\text{Cd}^{2+}$  and  $\text{Ca}^{2+}$  (b) in the solution vs. time.

ion exchange with  $\text{Pb}^{2+}$  and the hydrolysis of tobermorite in the acidic solution. The tobermorite has a sandwich-like structure that consists of a central layer of  $\text{CaO}$  octahedra with individual silicate “dreierketten” chains on each side, and the interlayer contains water, calcium, alkali and other ions [34]. Therefore,  $\text{Ca}^{2+}$  from the interlayer and the surface of tobermorite could exchange with  $\text{Pb}^{2+}$  and  $\text{Cd}^{2+}$  in the solution. At the same time,  $\text{Ca}^{2+}$  in the interlayer or on the surface of tobermorite could also be released in the solution due to the acidic nature of the solution.

Fig. 10 presents the XRD patterns of the  $\text{Pb}^{2+}$  adsorbed tobermorite (a) and the  $\text{Cd}^{2+}$  adsorbed tobermorite (b). The diffraction peaks of tobermorite decreased after adsorption of  $\text{Pb}^{2+}$  and  $\text{Cd}^{2+}$ , compared to the tobermorite before adsorption (Fig. 1). The reaction of tobermorite with  $\text{Pb}^{2+}$  and  $\text{Cd}^{2+}$  resulted in the precipitation of  $\text{PbCO}_3$  (ICDD card no. 01-070-2052) and  $\text{CdCO}_3$  (ICDD card no. 00-042-1342). This was consistent with the adsorption kinetics that the adsorption processes were governed by chemisorption. The phenomena reveal that the  $\text{Pb}^{2+}$  and  $\text{Cd}^{2+}$  were removed by tobermorite via chemical precipitation, because the  $\text{Ca}^{2+}$  of tobermorite was substituted by  $\text{Pb}^{2+}$  and  $\text{Cd}^{2+}$ , and the carbonization occurred during this process [53].

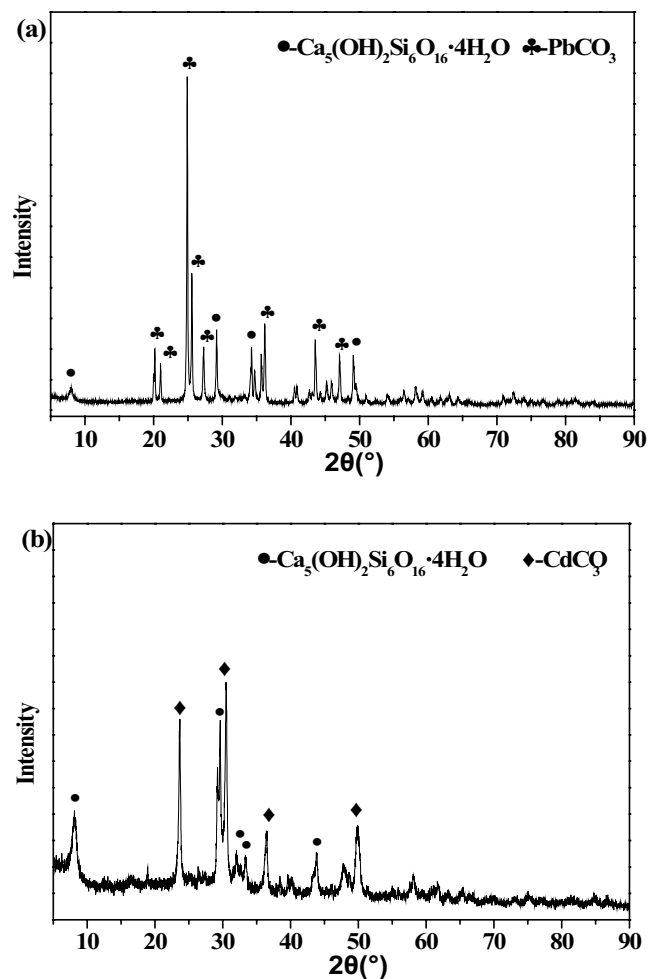


Fig. 10. XRD patterns of the  $\text{Pb}^{2+}$  adsorbed tobermorite (a) and the  $\text{Cd}^{2+}$  adsorbed tobermorite (b).

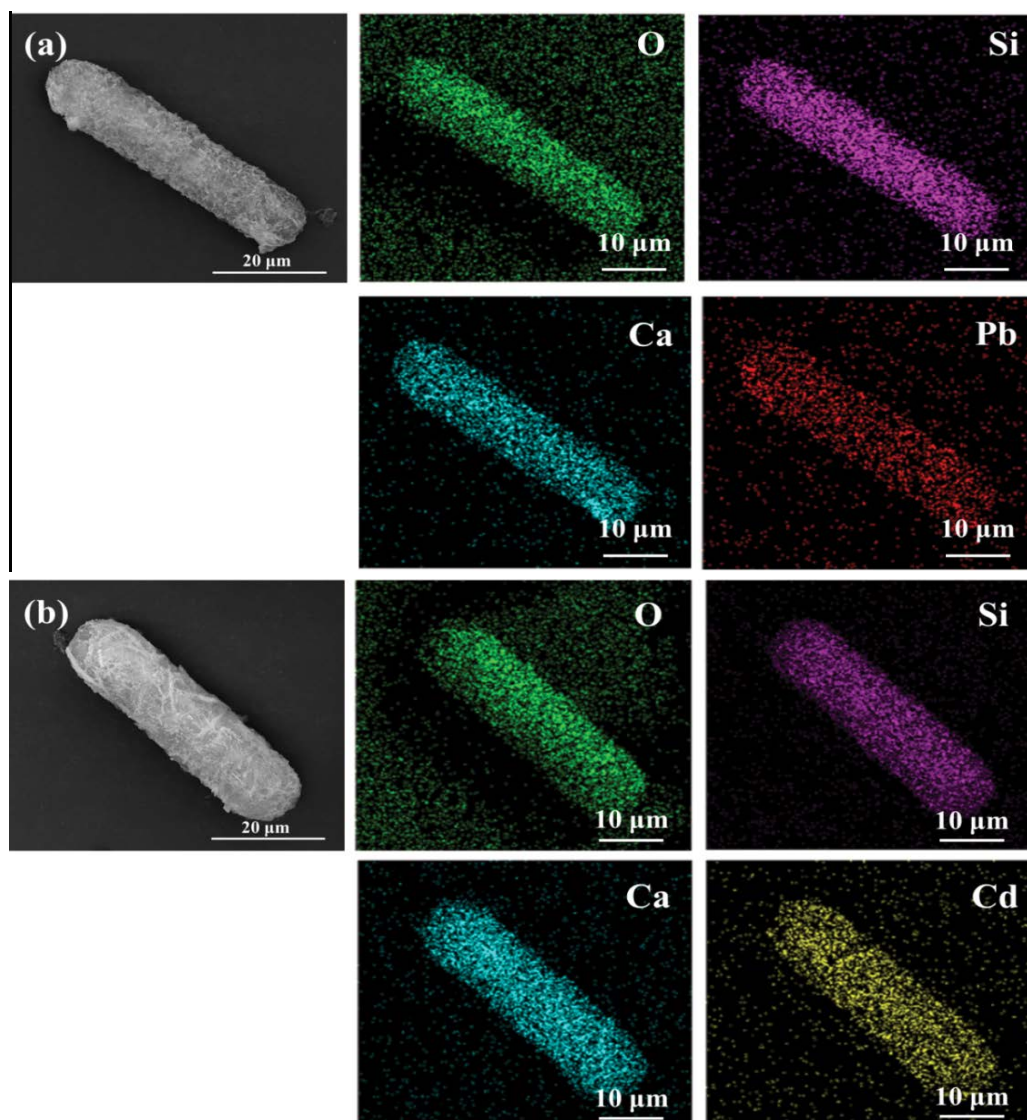


Fig. 11. SEM images and EDS elemental mappings of the Pb<sup>2+</sup> adsorbed tobermorite (a) and the Cd<sup>2+</sup> adsorbed tobermorite (b).

Fig. 11 illustrates the SEM images and EDS elemental mappings of the Pb<sup>2+</sup> adsorbed tobermorite (a,c) and the Cd<sup>2+</sup> adsorbed tobermorite (b,d). Fig. 11 shows the morphologies of the Pb<sup>2+</sup> adsorbed tobermorite and the Cd<sup>2+</sup> adsorbed tobermorite were porous rodlike particles. When compared to the morphology of the tobermorite before adsorption in Fig. 4a and b, there was no significant difference due to the high stability of the material. The EDS elemental mappings of the Pb<sup>2+</sup> adsorbed tobermorite and the Cd<sup>2+</sup> adsorbed tobermorite clearly present the appearance of Pb and Cd on the surface of the Pb<sup>2+</sup> adsorbed tobermorite and the Cd<sup>2+</sup> adsorbed tobermorite, respectively. This was consistent with the XRD results that Pb<sup>2+</sup> and Cd<sup>2+</sup> were adsorbed on the surface of tobermorite through surface complexation, ion exchange, or precipitation.

Fig. 12 shows the XPS spectra of the tobermorite, the Pb<sup>2+</sup> adsorbed tobermorite, and the Cd<sup>2+</sup> adsorbed tobermorite. The XPS spectra clearly show the presence of Pb

and Cd on the surface of tobermorite after adsorption. The binding energies for the Pb 4f<sub>7/2</sub> and Pb 4f<sub>5/2</sub> peaks are 138.05 and 142.8 eV, respectively, as shown in Fig. 12a, which were similar to those reported in the literature confirming the appearance of Pb on the surface of the Pb<sup>2+</sup> adsorbed tobermorite [54–56]. As shown in Fig. 12b, the binding energies for the Cd 3d<sub>3/2</sub> and Cd 3d<sub>5/2</sub> peaks are 412.2 and 405.35 eV, respectively, which were similar to those reported in the literature confirming the appearance of Cd on the surface of the Cd<sup>2+</sup> adsorbed tobermorite [50]. Consequently, it reveals that the adsorption of Pb<sup>2+</sup> and Cd<sup>2+</sup> on tobermorite occurred through surface complexation, the ion exchange with Ca<sup>2+</sup>, or precipitation on the surface of tobermorite.

Based on the above analyses, the mechanisms for the Pb<sup>2+</sup> and Cd<sup>2+</sup> adsorption on tobermorite synthesized from AEFA were complex, as shown in Fig. 13. First of all, the high specific surface area and the mesoporous structure of the tobermorite contributed to the adsorption of Pb<sup>2+</sup> and

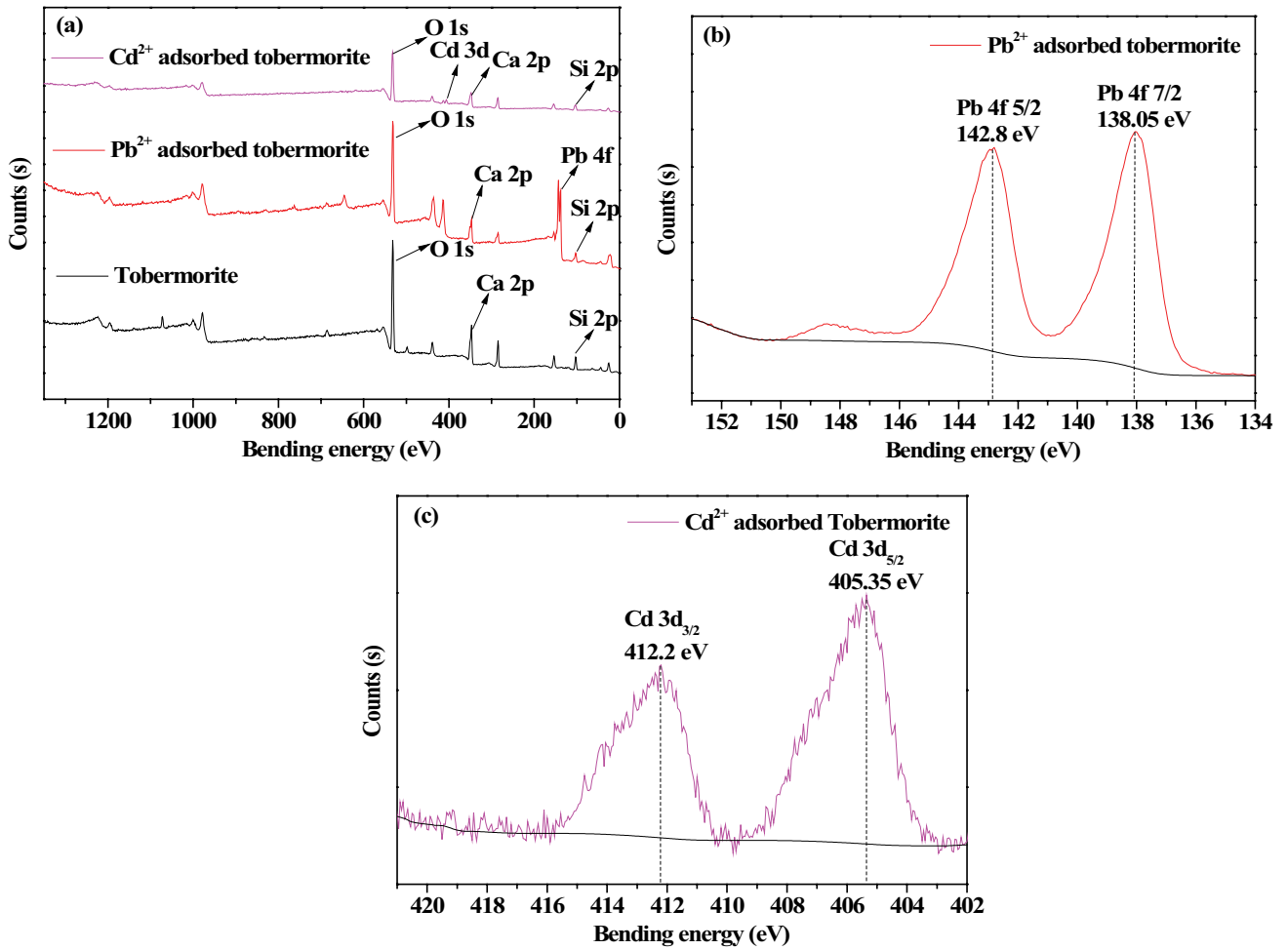


Fig. 12. XPS spectra of the tobermorite, the  $Pb^{2+}$  adsorbed tobermorite and the  $Cd^{2+}$  adsorbed tobermorite: full range (a),  $Pb\ 4f$  (b), and  $Cd\ 3d$  (c).

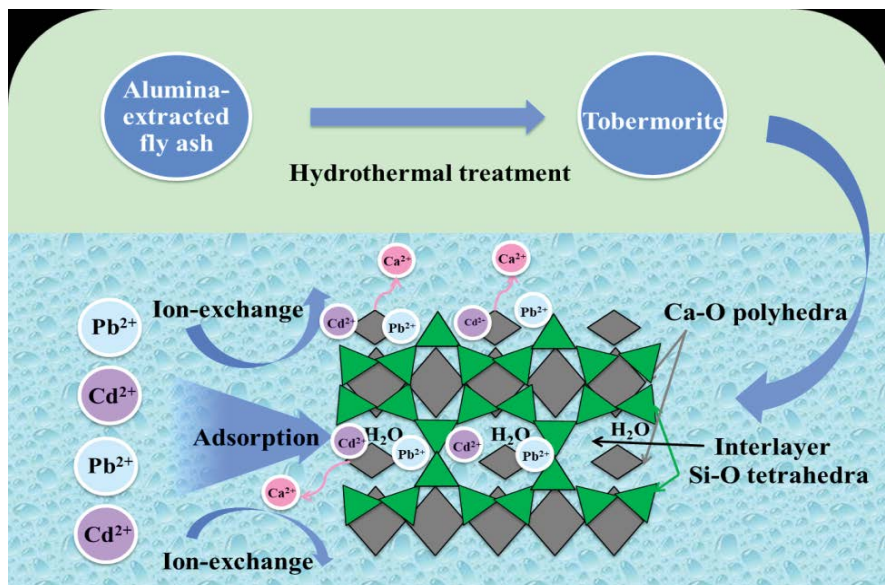


Fig. 13. Schematic presentation of the adsorption mechanisms of the tobermorite towards  $Pb^{2+}$  and  $Cd^{2+}$ .

Cd<sup>2+</sup>. Secondly, the Pb<sup>2+</sup> and Cd<sup>2+</sup> could be adsorbed by tobermorite through surface complexation or ion exchange with the Ca<sup>2+</sup> from the surface of tobermorite. Thirdly, the precipitation of PbCO<sub>3</sub> and CdCO<sub>3</sub> occurred on the surface of tobermorite. Finally, Pb<sup>2+</sup> and Cd<sup>2+</sup> could also exchange with the Ca<sup>2+</sup> from the interlayer and the structure of tobermorite. Above all, the Pb<sup>2+</sup> and Cd<sup>2+</sup> ions diffused into the mesoporous structure of the tobermorite and exchanged with more Ca<sup>2+</sup>, forming the precipitation of PbCO<sub>3</sub> and CdCO<sub>3</sub>, which led to the high adsorption capacity of Pb<sup>2+</sup> and Cd<sup>2+</sup>.

#### 4. Conclusions

In summary, a mesoporous tobermorite was successfully synthesized from AEFA by a facile hydrothermal method, with a high specific surface area of 68.4 m<sup>2</sup> g<sup>-1</sup> and a pore volume of 0.19 cm<sup>3</sup> g<sup>-1</sup>. The tobermorite particles presented aggregates of plate-like particles resulting in slit-shaped pores. The mesoporous tobermorite showed high removal efficiencies for Pb<sup>2+</sup> and Cd<sup>2+</sup> of 99.97% and 78.64%, respectively, and the adsorption kinetic data for Pb<sup>2+</sup> and Cd<sup>2+</sup> on tobermorite were better fitted to the pseudo-second-order kinetic model, revealing the adsorption processes were governed by chemisorption. The Pb<sup>2+</sup> and Cd<sup>2+</sup> adsorption isotherms were better described by the Langmuir isotherm model, suggesting monolayer adsorption, and the maximum adsorption capacities of the tobermorite towards Pb<sup>2+</sup> and Cd<sup>2+</sup> were 338.98 and 105.37 mg g<sup>-1</sup>, respectively. The mechanisms for the Pb<sup>2+</sup> and Cd<sup>2+</sup> adsorption on tobermorite were due to the high specific surface area of tobermorite, the ion exchange of Ca<sup>2+</sup> with Pb<sup>2+</sup> and Cd<sup>2+</sup>, and the precipitation of PbCO<sub>3</sub> and CdCO<sub>3</sub>. The high adsorption capacities for Pb<sup>2+</sup> and Cd<sup>2+</sup> on the tobermorite indicate that the mesoporous tobermorite synthesized from AEFA has a good application prospect as a low-cost and effective adsorbent for Pb<sup>2+</sup> and Cd<sup>2+</sup> in wastewater.

#### Acknowledgments

The authors gratefully acknowledge the financial support from the National Natural Science Foundation of China (No. 52004128, No. 51774261), and the Project of Reinforcing School with Innovation of the Department of Education of Guangdong Province (2018KZDXM051).

#### References

- [1] C.B. Godiya, L.A.M. Ruotolo, W. Cai, Functional biobased hydrogels for the removal of aqueous hazardous pollutants: current status, challenges, and future perspectives, *J. Mater. Chem. A*, 8 (2020) 21585–21612.
- [2] L. Järup, Hazards of heavy metal contamination, *Br. Med. Bull.*, 68 (2003) 167–182.
- [3] P.B. Tchounwou, C.G. Yedjou, A.K. Patlolla, D.J. Sutton, Heavy metals toxicity and the environment, *Mol. Clin. Environ. Toxicol.*, 101 (2012) 133–164.
- [4] A. Heidari, H. Younesi, Z. Mehraban, Removal of Ni(II), Cd(II), and Pb(II) from a ternary aqueous solution by amino functionalized mesoporous and nano mesoporous silica, *Chem. Eng. J.*, 153 (2009) 70–79.
- [5] F. Fu, Q. Wang, Removal of heavy metal ions from wastewaters: a review, *J. Environ. Manage.*, 92 (2011) 407–418.
- [6] C. Fan, K. Li, J. Li, D. Ying, Y. Wang, J. Jia, Comparative and competitive adsorption of Pb(II) and Cu(II) using tetraethylenepentamine modified chitosan/CoFe<sub>2</sub>O<sub>4</sub> particles, *J. Hazard. Mater.*, 326 (2017) 211–220.
- [7] S. Muthusarayanan, N. Sivarajasekar, J. Vivek, T. Paramasivan, M. Naushad, J. Prakashmaran, V. Gayathri, O.K. Al-Duaij, Phytoremediation of heavy metals: mechanisms, methods and enhancements, *Environ. Chem. Lett.*, 16 (2018) 1339–1359.
- [8] G. Sharma, D. Pathania, M. Naushad, N. Kothiyal, Fabrication, characterization and antimicrobial activity of polyaniline Th(IV) tungstomolybdophosphate nanocomposite material: efficient removal of toxic metal ions from water, *Chem. Eng. J.*, 251 (2014) 413–421.
- [9] A.E. Burakov, E.V. Galunin, I.V. Burakova, A.E. Kucherova, S. Agarwal, A.G. Tkachev, V.K. Gupta, Adsorption of heavy metals on conventional and nanostructured materials for wastewater treatment purposes: a review, *Ecotoxicol. Environ. Saf.*, 148 (2018) 702–712.
- [10] T.K. Naiya, A.K. Bhattacharya, S.K. Das, Adsorption of Cd(II) and Pb(II) from aqueous solutions on activated alumina, *J. Colloid Interface Sci.*, 333 (2009) 14–26.
- [11] A. Rahmani, H.Z. Mousavi, M. Fazli, Effect of nanostructure alumina on adsorption of heavy metals, *Desalination*, 253 (2010) 94–100.
- [12] Y.-H. Li, S. Wang, J. Wei, X. Zhang, C. Xu, Z. Luan, D. Wu, B. Wei, Lead adsorption on carbon nanotubes, *Chem. Phys. Lett.*, 357 (2002) 263–266.
- [13] M.A. Tofighty, T. Mohammadi, Adsorption of divalent heavy metal ions from water using carbon nanotube sheets, *J. Hazard. Mater.*, 185 (2011) 140–147.
- [14] Z. Huang, X. Zheng, W. Lv, M. Wang, Q. Yang, F. Kang, Adsorption of lead(II) ions from aqueous solution on low-temperature exfoliated graphene nanosheets, *Langmuir*, 27 (2011) 7558–7562.
- [15] Z. Han, Z. Tang, S. Shen, B. Zhao, G. Zheng, J. Yang, Strengthening of graphene aerogels with tunable density and high adsorption capacity towards Pb<sup>2+</sup>, *Sci. Rep.*, 4 (2014) 5025, doi: 10.1038/srep05025.
- [16] J. Goel, K. Kadirvelu, C. Rajagopal, V.K. Garg, Removal of lead(II) by adsorption using treated granular activated carbon: batch and column studies, *J. Hazard. Mater.*, 125 (2005) 211–220.
- [17] M. Momcilovic, M. Purenovic, A. Bojic, A.R. Zarubica, M.S. Randelovic, Removal of lead(II) ions from aqueous solutions by adsorption onto pine cone activated carbon, *Desalination*, 276 (2011) 53–59.
- [18] S. Wang, T. Terdkiatburana, M. Tadé, Adsorption of Cu(II), Pb(II) and humic acid on natural zeolite tuff in single and binary systems, *Sep. Purif. Technol.*, 62 (2008) 64–70.
- [19] X. Wang, D. Shao, G. Hou, X. Wang, A. Alsaedi, B. Ahmad, Uptake of Pb(II) and U(VI) ions from aqueous solutions by the ZSM-5 zeolite, *J. Mol. Liq.*, 207 (2015) 338–342.
- [20] M.J.K. Ahmed, M. Ahmaruzzaman, A review on potential usage of industrial waste materials for binding heavy metal ions from aqueous solutions, *J. Water Process Eng.*, 10 (2016) 39–47.
- [21] S. Babel, T.A. Kurniawan, Low-cost adsorbents for heavy metals uptake from contaminated water: a review, *J. Hazard. Mater.*, 97 (2003) 219–243.
- [22] Z. Yao, X. Ji, P. Sarker, J. Tang, L. Ge, M. Xia, Y. Xi, A comprehensive review on the applications of coal fly ash, *Earth-Sci. Rev.*, 141 (2015) 105–121.
- [23] J. Ding, S. Ma, S. Shen, Z. Xie, S. Zheng, Y. Zhang, Research and industrialization progress of recovering alumina from fly ash: a concise review, *Waste Manage.*, 60 (2017) 375–387.
- [24] S. Dai, L. Zhao, S. Peng, C.-L. Chou, X. Wang, Y. Zhang, D. Li, Y. Sun, Abundances and distribution of minerals and elements in high-alumina coal fly ash from the Jungar Power Plant, Inner Mongolia, China, *Int. J. Coal Geol.*, 81 (2010) 320–332.
- [25] L. Qi, Y. Yuan, Characteristics and the behavior in electrostatic precipitators of high-alumina coal fly ash from the Jungar power plant, Inner Mongolia, China, *J. Hazard. Mater.*, 192 (2011) 222–225.
- [26] Q. Yang, S. Ma, S. Zheng, R. Zhang, Recovery of alumina from circulating fluidized bed combustion Al-rich fly ash using mild hydrochemical process, *Trans. Nonferrous Met. Soc. China*, 24 (2014) 1187–1195.

- [27] J. Ding, S. Ma, S. Zheng, Y. Zhang, Z. Xie, S. Shen, Z. Liu, Study of extracting alumina from high-alumina PC fly ash by a hydro-chemical process, *Hydrometallurgy*, 161 (2016) 58–64.
- [28] Z. Wang, S. Ma, Z. Tang, X. Wang, S. Zheng, Effects of particle size and coating on decomposition of alumina-extracted residue from high-alumina fly ash, *J. Hazard. Mater.*, 308 (2016) 253–263.
- [29] Z. Wang, S. Zheng, S. Ma, J. Ding, X. Wang, Recovery of sodium from alumina-extracted fly ash using concentrated sodium carbonate solution, *J. Min. Metall.*, 54 (2018) 225–232.
- [30] N.J. Coleman, Interactions of Cd(II) with waste-derived 11 Å tobermorite s, *Sep. Purif. Technol.*, 48 (2006) 62–70.
- [31] H. Luo, D. He, W. Zhu, Y. Wu, Z. Chen, E.-H. Yang, Humic acid-induced formation of tobermorite upon hydrothermal treatment with municipal solid waste incineration bottom ash and its application for efficient removal of Cu(II) ions, *Waste Manage.*, 84 (2019) 83–90.
- [32] Z. Zhao, J. Wei, F. Li, X. Qu, L. Shi, H. Zhang, Q. Yu, Synthesis, Characterization and hexavalent chromium adsorption characteristics of aluminum- and sucrose-incorporated tobermorite, *Materials*, 10 (2017) 597, doi: 10.3390/ma10060597.
- [33] T. Tsutsumi, S. Nishimoto, Y. Kameshima, M. Miyake, Hydrothermal preparation of tobermorite from blast furnace slag for Cs<sup>+</sup> and Sr<sup>2+</sup> sorption, *J. Hazard. Mater.*, 266 (2014) 174–181.
- [34] Z. Wang, S. Ma, S. Zheng, X. Wang, Incorporation of Al and Na in hydrothermally synthesized tobermorite, *J. Am. Ceram. Soc.*, 100 (2017) 792–799.
- [35] S. Azizian, Kinetic models of sorption: a theoretical analysis, *J. Colloid Interface Sci.*, 276 (2004) 47–52.
- [36] Y. Ho, Review of second-order models for adsorption systems, *J. Hazard. Mater.*, 136 (2006) 681–689.
- [37] C.A. Coles, R.N. Yong, Aspects of kaolinite characterization and retention of Pb and Cd, *Appl. Clay Sci.*, 22 (2002) 39–45.
- [38] C.A. Christophi, L. Axe, Competition of Cd, Cu, and Pb adsorption on goethite, *J. Environ. Eng.*, 126 (2000) 66–74.
- [39] T. Wang, W. Liu, L. Xiong, N. Xu, J. Ni, Influence of pH, ionic strength and humic acid on competitive adsorption of Pb(II), Cd(II) and Cr(III) onto titanate nanotubes, *Chem. Eng. J.*, 215 (2013) 366–374.
- [40] X.S. Wang, H.H. Miao, W. He, H.L. Shen, Competitive adsorption of Pb(II), Cu(II), and Cd(II) ions on wheat-residue derived black carbon, *J. Chem. Eng. Data*, 56 (2011) 444–449.
- [41] M.R. Awual, M.M. Hasan, A ligand based innovative composite material for selective lead(II) capturing from wastewater, *J. Mol. Liq.*, 294 (2019) 111679, doi: 10.1016/j.molliq.2019.111679.
- [42] M. Naushad, Z. AlOthman, M.R. Awual, M.M. Alam, G. Eldesoky, Adsorption kinetics, isotherms, and thermodynamic studies for the adsorption of Pb<sup>2+</sup> and Hg<sup>2+</sup> metal ions from aqueous medium using Ti(IV) iodovanadate cation exchanger, *Ionics*, 21 (2015) 2237–2245.
- [43] I. Alinnor, Adsorption of heavy metal ions from aqueous solution by fly ash, *Fuel*, 86 (2007) 853–857.
- [44] S. Wang, T. Terdkiatburana, M. Tadé, Single and co-adsorption of heavy metals and humic acid on fly ash, *Sep. Purif. Technol.*, 58 (2008) 353–358.
- [45] M. Visa, Synthesis and characterization of new zeolite materials obtained from fly ash for heavy metals removal in advanced wastewater treatment, *Powder Technol.*, 294 (2016) 338–347.
- [46] K. He, Y. Chen, Z. Tang, Y. Hu, Removal of heavy metal ions from aqueous solution by zeolite synthesized from fly ash, *Environ. Sci. Pollut. Res.*, 23 (2016) 2778–2788.
- [47] N.J. Coleman, D.S. Brassington, Synthesis of Al-substituted 11 Å tobermorite from newsprint recycling residue: a feasibility study, *Mater. Res. Bull.*, 38 (2003) 485–497.
- [48] I. Kula, M. Uğurlu, H. Karaoğlu, A. Celik, Adsorption of Cd(II) ions from aqueous solutions using activated carbon prepared from olive stone by ZnCl<sub>2</sub> activation, *Bioresour. Technol.*, 99 (2008) 492–501.
- [49] A. Papandreou, C. Stourmaras, D. Pnias, Copper and cadmium adsorption on pellets made from fired coal fly ash, *J. Hazard. Mater.*, 148 (2007) 538–547.
- [50] X. Huang, H. Zhao, G. Zhang, J. Li, Y. Yang, P. Ji, Potential of removing Cd(II) and Pb(II) from contaminated water using a newly modified fly ash, *Chemosphere*, 242 (2020) 125148, doi: 10.1016/j.chemosphere.2019.125148.
- [51] T.C. Nguyen, P. Loganathan, T.V. Nguyen, S. Vigneswaran, J. Kandasamy, R. Naidu, Simultaneous adsorption of Cd, Cr, Cu, Pb, and Zn by an iron-coated Australian zeolite in batch and fixed-bed column studies, *Chem. Eng. J.*, 270 (2015) 393–404.
- [52] G. Sharma, M. Naushad, Adsorptive removal of noxious cadmium ions from aqueous medium using activated carbon/zirconium oxide composite: isotherm and kinetic modelling, *J. Mol. Liq.*, 310 (2020) 113025, doi: 10.1016/j.molliq.2020.113025.
- [53] X. Guo, H. Shi, Microstructure and heavy metal adsorption mechanisms of hydrothermally synthesized Al-substituted tobermorite, *Mater. Struct.*, 50 (2017) 245, doi: 10.1617/s11527-017-1100-0.
- [54] V.G.R. Chada, D.B. Hausner, D.R. Strongin, A.A. Rouff, R.J. Reeder, Divalent Cd and Pb uptake on calcite {1014} cleavage faces: an XPS and AFM study, *J. Colloid Interface Sci.*, 288 (2005) 350–360.
- [55] H. Abdel-Samad, P.R. Watson, An XPS study of the adsorption of lead on goethite ( $\alpha$ -FeOOH), *Appl. Surf. Sci.*, 136 (1998) 46–54.
- [56] T. Yoshida, T. Yamaguchi, Y. Iida, S. Nakayama, XPS study of Pb(II) adsorption on  $\gamma$ -Al<sub>2</sub>O<sub>3</sub> surface at high pH conditions, *J. Nucl. Sci. Technol.*, 40 (2003) 672–678.